FlatChem 33 (2022) 100366

Contents lists available at ScienceDirect

FlatChem

journal homepage: www.sciencedirect.com/journal/flatchem

Room-temperature emitters in wafer-scale few-layer hBN by atmospheric pressure CVD

João Fernandes [a,1], Tiago Queirós [b,e,1], João Rodrigues [a], Siva Sankar Nemala [a], Alec P. LaGrow [c], Ernesto Placidi [d], Pedro Alpuim [a,e], Jana B. Nieder [b], Andrea Capasso [a,*]

[a] 2D Materials and Devices Group, International Iberian Nanotechnology Laboratory, 4715-330 Braga, Portugal
[b] Ultrafast Bio- and Nanophotonics Group, International Iberian Nanotechnology Laboratory, 4715-330 Braga, Portugal
[c] AEMIS Facility, International Iberian Nanotechnology Laboratory, 4715-330 Braga, Portugal
[d] Dipartimento di Fisica, Università di Roma La Sapienza, 00185 Rome, Italy
[e] Centro de Física das Universidades do Minho e do Porto, Universidade do Minho, 4710-057 Braga, Portugal

ARTICLE INFO

Keywords:
2D material
Hexagonal boron nitride
Atmospheric-pressure chemical vapor deposition
Single-photon emitters

ABSTRACT

Hexagonal boron nitride (hBN) is a two-dimensional, wide band gap semiconductor material suitable for several technologies. 2D hBN appeared as a viable platform to produce bright and optically stable single photon emitters (SPEs) at room temperature, which are in demand for quantum technologies. In this context, one main challenge concerns the upscaling of 2D hBN with uniform spatial and spectral distribution of SPE sources. In this work we optimized the atmospheric-pressure chemical vapor deposition (APCVD) growth and obtained large-area 2D hBN with uniform fluorescence emission properties. We characterized the hBN films by a combination of electron microscopy, Raman and X-ray photoelectron spectroscopy techniques. The extensive characterization revealed few-layer, polycrystalline hBN films (~3 nm thickness) with balanced stoichiometry and uniformity over 2″ wafer scale. We studied the fluorescence emission properties of the hBN films by multidimensional hyperspectral fluorescence microscopy. We measured simultaneously the spatial position, intensity, and spectral properties of the emitters, which were exposed to continuous illumination over minutes. Three main emission peaks (at 538, 582, and 617 nm) were observed, with associated replica peaks red-shifted by ~53 nm. A surface emitter density of ~0.1 emitters/μm^2 was found. A comparative test with pristine hBN nanosheets produced by liquid-phase exfoliation (LPE) was performed, finding that CVD and LPE hBN possess analogous spectral emitter categories in terms of peak position/intensity and density. Overall, the line-shape and wavelength of the emission peaks, as well as the other measured features, are consistent with single-photon emission from hBN. The results indicate that APCVD hBN might proficiently serve as a SPE platform for quantum technologies.

Introduction

Research on two-dimensional materials (2DM) has progressed steadily in recent years [1]. 2DMs have a variety of outstanding optical, electronic, and mechanical properties that look ideal for a diverse range of (opto)electronic technologies [2–4]. 2D hexagonal boron nitride (hBN) is a III–V layered material with insulating electrical properties (bandgap of ~6 eV) [5,6]. Its characteristics, combined with a ultra-flat surface and highly stable structure, make 2D hBN a potential building block in several technologies, such as field effect transistors, tunneling devices, deep ultraviolet emitters and detectors, and photoelectric devices [7–10]. Recently, 2D hBN demonstrated potential towards quantum technologies by showing single-photon emission (SPE) [11,12]. In this context, an ideal solid-state system should display atomic-like states, which can be prepared in a reproducible manner and read-out optically [13,14]. Differently from other SPE materials (such as diamond, quantum dots, and a few transition metal dichalcogenides), 2D hBN has shown bright, visible SPE at room temperature [15]. This fact, together with high light collection efficiency and easy integration in photonic circuits, makes 2D hBN a viable platform for information processing, computing, and metrological applications [13,16].

The emission in 2D hBN has been compared to that of diamond,

* Corresponding author.
E-mail address: andrea.capasso@inl.int (A. Capasso).
[1] These authors contributed equally.

https://doi.org/10.1016/j.flatc.2022.100366
Received 18 February 2022; Received in revised form 31 March 2022; Accepted 12 April 2022
Available online 15 April 2022

where the narrow-band visible emission is due to an atomic-scale point defect, *i.e.*, N vacancy centers [17]. It has been proposed that the emissive defect state in hBN should be either a B or N vacancy, or an antisite complex, in which a B atom is replaced by a N atom not having a neighboring N atom [11]. In the past few years, extensive research on single-photon emitters in hBN was conducted, but marked progress toward device integration has been hindered by the high variation in the emission frequency, which can be attributed to the host of heterogeneous 2D hBN samples produced so far [18,19]. The vast majority of optical studies have been carried out on mechanically exfoliated [20,21] or liquid [11,18] hBN samples, which are usually multilayers lacking a well-defined morphology or thickness (which is known to strongly affect the band structure of hBN [22]). Such samples were produced by a variety of different conditions and, as such, likely contained a wider range of structural defects than those produced by chemical vapor deposition (CVD) [18,21]. CVD has thus been identified as the most suitable method to produce hBN with well-defined thickness over large areas, thus allowing the investigation into the optical properties of large crystalline 2D domains. Several CVD approaches to produce the ideal hBN SPE platform have been proposed: This platform should possess homogeneous defect types (and thus emission spectra), high emitter density with sufficient inter-emitter spacing for identifiable emission, and a stable emitter fluorescence intermittency. Recently, high SPE density in atomic-thick CVD hBN has been reported in a few cases [23,24]. Controllable, versatile and inexpensive CVD processes for the production of 2D hBN still appear essential to produce and exploit identifiable SPE sources in devices.

The CVD of atomic-thick hBN still presents three main challenges; i) reducing/suppressing the crystal impurity and defect level, ii) synthesizing large-scale and homogeneous samples and iii) controlling the thickness of the materials to be grown. Whereas there are other difficulties concerning the transfer method, which should ideally avoid the introduction of any further defects, impurities, or cracks. Several CVD precursors were proposed to grow hBN thin films: gaseous (*e.g.*, boron trifluoride, boron trichloride, diborane and ammonia) [25], liquid (*e.g.*, borazine, molten $Fe_{82}B_{12}$ alloy) [26,27], and solid (*e.g.*, ammonia borane – AB) [28]. Borazine is one of the most common precursors, due to its high vapor pressure. However, this compound is toxic, highly flammable, and difficult to store, thus presenting obvious safety concerns. hBN thin films can be grown from mixtures of diborane and ammonia, but diborane is also toxic and pyrophoric. By contrast, AB is a non-hazardous and inexpensive hBN precursor. Regarding the catalytic substrates, several metals (*i.e.*, Ru, Ni, Rh, Pt and Cu) were tested, each one with distinct parameters such as composition, lattice symmetry and constant, and electronic structure [29]. High binding energy and good lattice match are usually preferable in a CVD substrate. The price of the substrates is also relevant, de-facto excluding the choice of metals as Rh and Pt for industrial production, as an example. Ni and Cu have relatively high binding energies and a lattice mismatch with hBN of 0.4% and 0.9%, respectively: These features and a reasonable cost make them the most suitable substrates for hBN growth [30].

In this work, we propose a simple, low-cost and reproducible process to produce high-quality hBN by atmospheric pressure chemical vapor deposition (APCVD) for quantum technologies. By a series of optimization steps, we obtained uniform, few-layer hBN films over large areas (*i.e.*, up to 20 cm^2). Although the use of low pressure chemical vapor deposition (LPCVD) is usually associated with a higher hBN quality (along with higher control in thickness and uniformity) [31], we achieved an analogous sample quality by a more versatile approach. Overall, our method entails lower operating and maintenance costs, more suitable for industrial purposes. We studied the viability of our CVD hBN as a SPE platform. Two highly sensitive fluorescence microscopy techniques (*i.e.*, total internal reflection and spectrally resolved confocal) were used to this end. Also, we cross-checked our measurements on CVD hBN with those acquired on samples made by liquid phase exfoliation (LPE). Individual and widespread fluorescent emitters were measured, which shared comparable spectral properties and same order of densities in both kinds of samples. The photonic performance of APCVD hBN makes this material accessible for quantum technology.

Experimental

Atmospheric pressure CVD growth of hBN films

The growth of hBN films was carried out in a two-zone split tube furnace (2″ quartz tube) at atmospheric pressure. 25 μm thick Cu foils (cut in rectangles, with an area up to 2 × 10 cm^2) were used as substrates. Prior to deposition, the substrate was cleaned in an aqueous solution (280 mL deionized water, 10 mL HCl 37%, 2.5 mL 2 M $FeCl_3$) for 1 min in an ultrasonic bath, and then rinsed in deionized water. The substrate was then dried with N_2 flow, placed on a cleaned Si/SiO_2 holder and loaded into the second heating zone of the furnace. 8.5 mg of AB was placed in an Al holder and loaded in the first heating zone of the furnace (45 cm upstream from the substrate). The tube was purged for 20 min under an Ar/H_2 flow (100 sccm of a mixture of 95% Ar and 5% H_2). After the purge, the second heating zone was ramped up to 1020 °C (40 °C/min) to anneal the Cu substrate (40 min at 1020 °C under the same Ar/H_2 mixture). After the annealing step, the Cu substrate was allowed to cool down to room temperature by opening the furnace lid. The first heating zone was heated up to begin the AB pre-treatment. Several pre-treatment conditions were tested such as: temperature, 80–100 °C; time, 150–180 min; Ar/H_2 flow (95/5%), 5, 15 and 100 sccm. The corresponding results are shown in the following sections. Once the AB pre-treatment was completed, the first heating zone was kept in the same pre-treatment conditions, and the second heating zone was ramped up to 1020 °C (40 °C/min) for the hBN growth, which lasted for 30 min under 100 sccm Ar/H_2 flow (95/5%). After the growth, both furnaces were turned off and allowed to cool down to room temperature before retrieving the samples for further characterization.

Polymer-assisted transfer process of hBN onto substrates

The hBN films were transferred onto SiO_2/Si substrates by PMMA-assisted method [32]. A layer of PMMA was spin-coated on the Cu/hBN sample. The Cu backside was cleaned via O_2 plasma (250 sccm O_2 flow, 0.4 mbar, eight consecutive cycles of 30 s plasma exposure, 200 W RF power) to remove the adventitious hBN. The cleaned Cu/hBN/PMMA sample was placed in a 0.2 M $FeCl_3$ solution for 2 h to etch away the Cu. After the etching, the freestanding hBN/PMMA sample was rinsed in deionized water several times and scooped out of the water bath with a Si/SiO_2 substrate (and then dried on a hot plate at 65 °C for 30 min). The sample was soaked in an acetone bath overnight to remove the PMMA coating. Finally, the sample was rinsed in IPA and deionized water (15 min each), and dried gently under N_2 flow. This same transfer process was used to transfer hBN onto 170 μm thick borosilicate glass cover slips for optical microscopy and further measurements.

Liquid phase exfoliation (LPE) of hBN flakes

1 g of hBN crystals (Sigma Aldrich, powder, ~1 μm, 98%) were dispersed in 400 mL of isopropanol (IPA) and stirred at 500 rpm for 30 min. The dispersion was shear-mixed at 5000 rpm for 6 h (keeping the beaker in an ice bath) and then centrifuged at 7000 rpm for 15 min to remove aggregated and unexfoliated flakes. The hBN dispersion was sonicated for 30 min before depositing 100 μL on each substrate (and drying for 10 min on a hotplate at 50 °C) for the measurements.

Sample characterization

Optical characterization

Images were acquired using a Motic PSM-1000 microscope with three lenses (10x, 50x and 100x) and a mechanical stage. Digital images

were recorded with a Moticam 5 + and the Motic Images Plus application software.

Confocal Raman microscopy

A ALPHA300 R Confocal Raman Microscope (WITec) with a 532 nm laser was used. The laser beam was focused on the sample by 50x and 100x lenses; single acquisitions and mappings were performed with 15 mW laser power (600 g/mm grating).

Atomic-force microscopy (AFM)

The thickness and morphology of the samples were measured in tapping mode with a Bruker Dimension ICON. Image processing was done with Gwyddion software.

Scanning-electron microscopy

Images were taken with a FEI Quanta 650 FEG with a cold field electron source, at 5 kV accelerating voltage. The CVD samples were transferred on a Si substrate coated with a 3-nm Au layer (Kenosistec UHV Sputtering).

X-ray photoelectron spectroscopy (XPS)

XPS data were acquired in ultra-high vacuum with a ESCALAB 250 Xi (Thermo Fisher Scientific). The base pressure in the system was below 5 x 10^{-10} mbar. The XPS spectra were generated by an Al monochromated X-ray source operated at 15 keV and 200 W power. The spectra were acquired with a hemispherical analyzer with pass energies of 200 and 20 eV for survey and high-resolution spectra, respectively.

(Scanning) transmission electron microscopy (STEM)

The hBN structure and composition was investigated with an aberration-corrected FEI Titan Cubed Themis (operated at 60 kV) equipped with X-FEG electron source, image corrector, probe corrector and Super-X EDS system. To characterize the crystal structure of hBN we used a combination of high resolution TEM (HRTEM), electron diffraction (ED) and high angle annular dark field (HAADF) STEM with energy dispersive X-ray spectroscopy (EDS). The HRTEM images were obtained with a monochromated beam with a potential of 3000 V. Electron energy loss spectroscopy (EELS) was also performed with an Enfinium GIF with an energy resolution of 1.0 eV.

Widefield total internal reflection fluorescence microscopy (TIRFM)

A Nikon Ti-E widefield TIRF microscope with a 488 nm laser at 25 mW power was used. Before any measurements were taken, the sample areas were cleaned by laser irradiation (10–15 min, same conditions) to decompose and remove potential contaminants (*e.g.*, superficially adsorbed molecules coming from the sample transfer and preparation processes), which might appear as emission spots. The fluorescence emission signals were collected with an oil immersion lens at 60x magnification and 1.4NA, and recorded with an integration time of 50 ms using an Andor IXon Ultra 897 EM-CCD camera. Widefield TIRF measurements were taken on sample areas of 138.2 by 138.2 μm^2. For each of these areas, four smaller regions of interest of 34.5 by 34.5 μm^2 were selected within the most focused part of the recordings. For image processing, the ThunderSTORM plugin in ImageJ was used to localize intensity spots of the size of the point spread function (PSF) and extract the locations of the fluorescent spots in the images. From the resulting coordinate table, the emitters with standard deviation of detection exceeding 50 nm (by the 2D Gaussian curve fitting process) were filtered out to ensure an accurate selection of the emitters.

Hyperspectral confocal fluorescence microscopy

A Zeiss LSM 780 confocal microscope, equipped with a 32-channel GaAsP detector for spectral imaging was used. An oil immersion objective of NA 1.4 and 63x magnification was used to collect the signal (in this way, the PSF of the system had a 220 nm FWHM for 488 nm wavelength). The spectral detection window across 32 channels of the detector was set to cover an emission wavelength ranging from 405 to 696 nm. Only the channels covering the range from 520 to 696 nm were considered for the analysis, to remove stray and scattered laser light. An Ar laser's emission line at 488 nm was used to excite the hBN samples at 12.5 mW average power. The hyperspectral image data were acquired pixel by pixel in laser scanning mode (from left to right, top to bottom). The signal was averaged 16 times with approximately 50 μs collection time per pixel (totaling an integration time of 0.8 ms per pixel). Zeiss Zen Black 3.0 software was used to perform linear unmixing of the recorded images, breaking down the data into three intensity maps (associated to the spectra found in the samples). ImageJ was used to segment these linear unmixed channels into signal and background via thresholding, and to perform a quantitative analysis of diffraction-limited spots, which were used to count the number of emitters per unit area. The "Analyze particles" method was used, which extracted a data table containing coordinates and shape descriptor values for all the identified spots. We specify that when automatically counting the SPE density, the "Analyze particles" algorithm could overestimate the count in the portion of the dataset with low signal to noise ratio (SNR). As described in the following section, some of the observed fluorescence spots appeared as a multitude of stripes or as half circles on areas matching the size of a single PSF, indicating the single defect center sensitivity reached.

Results

We performed an extensive optimization of the APCVD process, spanning from the substrate and precursor pre-treatments to the CVD parameters themselves. Initially, we tested several aqueous solutions to remove oxide and organic contaminants from the Cu substrate. In a surface-mediated process, the surface morphology of the substrate is particularly crucial [33]. An aqueous solution of deionized water, HCl and $FeCl_3$ resulted as an effective cleaning method (see Fig. S1 for details). The Cu substrate annealing at 1020 °C served to smoothen the Cu surface, and resulted crucial to the growth of a uniform film (see Fig. S2 for details). By controlling the solid-state phase transition of AB via heating, it is possible to maximize its volatility and control the sublimation [34,35]. To this end, we carefully controlled the pre-heating stage (in terms of temperature, precursor positioning and time) to release the gaseous precursor at the desired stage of the CVD process. Such AB pre-treatment was confirmed as a vital step for the deposition of high-quality hBN (Fig. S3). We further tuned the pre-treatment by testing three conditions: T = 80 °C for 180 min, T = 80 °C for 150 min, and T = 100 °C for 150 min. Fig. 1a-c show optical microscope images of the corresponding samples. The film in Fig. 1c appears as the smoothest of the three. The three Raman spectra (Fig. 1f-h) feature the E_{2g} peak at 1369 cm^{-1} typical of 2D hBN, and a peak at 1450 cm^{-1} originating from the Si substrate [36]. Remnant D and G carbon-related bands with different intensities are also visible, which could be attributed to minor carbon-containing contaminations [37]. In non-ideal conditions, the catalytic Cu substrate may react at high temperature with residual hydrocarbons (from the AB precursor or the tube environment) or solid carbon traces (emerging from the Cu foil), forming carbon-rich atomic clusters [38,39]. Among the three spectra, only the one in Fig. 1g does not show a Si vibration mode, indicating that the hBN film is the thickest of the three. The spectrum in Fig. 1h features the higher ratio between E_{2g} and Si-related peak, indicating a thin hBN film, having also a negligible carbon contamination. The influence of Ar + H_2 flow during the AB pre-treatment was also investigated, since non-ideal conditions could lead to undesired contamination [40]. Fig. 1d and e show optical micrographs of hBN films grown with 15 sccm and 5 sccm flow, respectively. Fig. 1i and j show the corresponding Raman spectra. The sample grown with 15 sccm of Ar + H_2 features a higher E_{2g} to Si-related peak ratio (when compared to Fig. 1h) indicating a thinner film. When reducing the flow to 5 sccm, the E_{2g} to Si-related peak ratio between remained high but the G band reduced, meaning that the carbon signal is now negligible. Regarding the AB pre-treatment, our tests indicated the

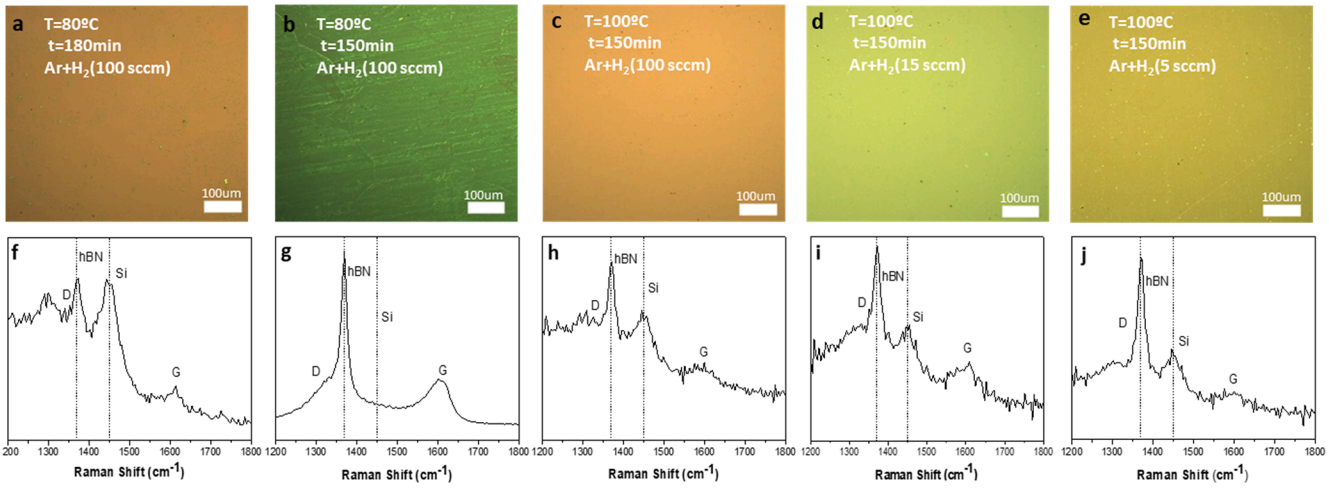

Fig. 1. a)-e) Optical images of the hBN films grown using different time, temperature and Ar + H_2 flow parameters during AB pre-treatment. d)-f) Raman plots of the corresponding films.

optimal combination is 100 °C under 5 sccm Ar/H_2 flow for 150 min.

After these optimization tests, we produced a series of atomically thin hBN samples with areas up to 20 cm^2. Portions of these films were transferred to a Si/SiO_2 substrate for characterization. The film edges are clearly visible in Fig. 2a and b, showing a clean interface between the hBN film and the substrate. A representative Raman spectrum is reported in Fig. 2c, where an intense E_{2g} peak at 1369 cm^{-1} and a weak peak at 1450 cm^{-1} appear [36]. A 900 μm^2 map of the E_{2g} peak is shown in Fig. 2d. The E_{2g} peak appears constant throughout the area indicating an atomic-thick, continuous and homogenous film. Only minor intensity fluctuations appear, possibly due to subtle thickness variations [41]. The darker, bottom-right corner of the map corresponds to the bare Si/SiO_2 substrate. The well-defined edges of the film allowed to perform very accurate AFM measurements, reporting an average thickness of ~3 nm (Fig. 2e) and a root mean square roughness of 3.5 nm. The close-up AFM image in Fig. 2f shows the typical wrinkles that appear in these films after the transfer process. The occasional presence of tiny white spots could also be noted. SEM images are reported in Fig. 2g and h. The different orientation of the underlying Cu grains can be observed, as well as the bright wrinkles of the hBN film [42].

Transmission electron microscopy (TEM) was performed to analyze the structure and composition of the hBN films. Fig. 3a shows the hBN film lying on the lacey carbon grid. The electron diffraction of the area (inset) is viewed down the [0 0 1] zone axis, with the bright reflections coming from a single orientation. Dimmer reflections around the ring show that there is a small fraction of the intensity coming from additional orientations, all of which are viewed down the 001 zone axis. Fig. 3b shows a high-resolution image of the hBN lattice, with four regions with different planar orientations. To better highlight the lattice structures, we isolated these different orientations in separate colors with an inverted FFT of the area (Fig. 3c). EELS was performed: The B and N maps in Fig. 3d resulted from integrating the intensity under each characteristic K-shell ionization. A homogenous overlap between the two components is apparent, highlighting the uniform distribution of B and N. The HRTEM analysis provides further details into the film structure. The edge analyzed in Fig. 3e reveals the few layers composing the film, with a perfect interlayer spacing of 3.3 Å. The close-up, top-view of the film in Fig. 3f highlights an area with three distinct thicknesses, attributed to one to three layers.

Energy dispersive X-ray spectroscopy (EDS) was employed to detect the presence of potential contaminations, possibly originated during the growth or the successive transfer process (Fig. 4a). The elemental distribution of N, B, Fe, Cl, and Si was mapped. The B and N maps (Fig. 4b and 4c) show the uniform presence of the main hBN elements in the film. An intensity contrast is visible in both maps, meaning that the area of analysis has different thicknesses. The Cu, Fe and Cl maps highlight that some residues arising from the transfer process can appear, as described in section 2.2. Fig. 4f confirm the presence of adventitious SiO_x nanoparticles (previously observed by AFM and SEM), which could be sub-μm SiO_x particles stemming from the interaction of evaporated Cu atoms and the inner walls of the quartz tube during the CVD process [39]. These particles could be suppressed by adding a confinement box and a screen in the tube-furnace to the CVD setup, as previously reported for graphene [43].

As detailed in the Introduction, hBN hosts bright and stable SPEs at room temperature making it suitable for quantum technologies. In particular, the large-area of our films is appealing because it allows further patterning or making arrays of emitters, which is desirable for practical applications [44]. In this regard, the SPE properties of the CVD hBN films were evaluated in the following sections. A comparative study was carried out by analyzing also an hBN sample produced via LPE (and deposited on glass, see Experimental). LPE is one of the main methods to obtain pristine, atomic-thick hBN for optoelectronics, and as such this could serve as a benchmark to assess the features of our CVD samples [45]. The LPE sample characterization shows aggregates of hBN flakes randomly distributed throughout the substrate (Fig. S4). The flakes appear as multilayer with a lateral size ranging from 50 to 200 nm. XPS was conducted to characterize the elemental stoichiometry of the two kinds of hBN samples. The surveys are reported in Fig. S5. High-resolution B1s and N1s spectra in Fig. 5 show the expected peak shapes and positions 190.9 and 398.2 eV, respectively. The N/B ratio is 1.18 for the CVD sample, and 1.16 for the LPE one, in good agreement with existing data [40,46]. We analyzed the spectra in detail, which could be fitted with three components each. The components at 191.1

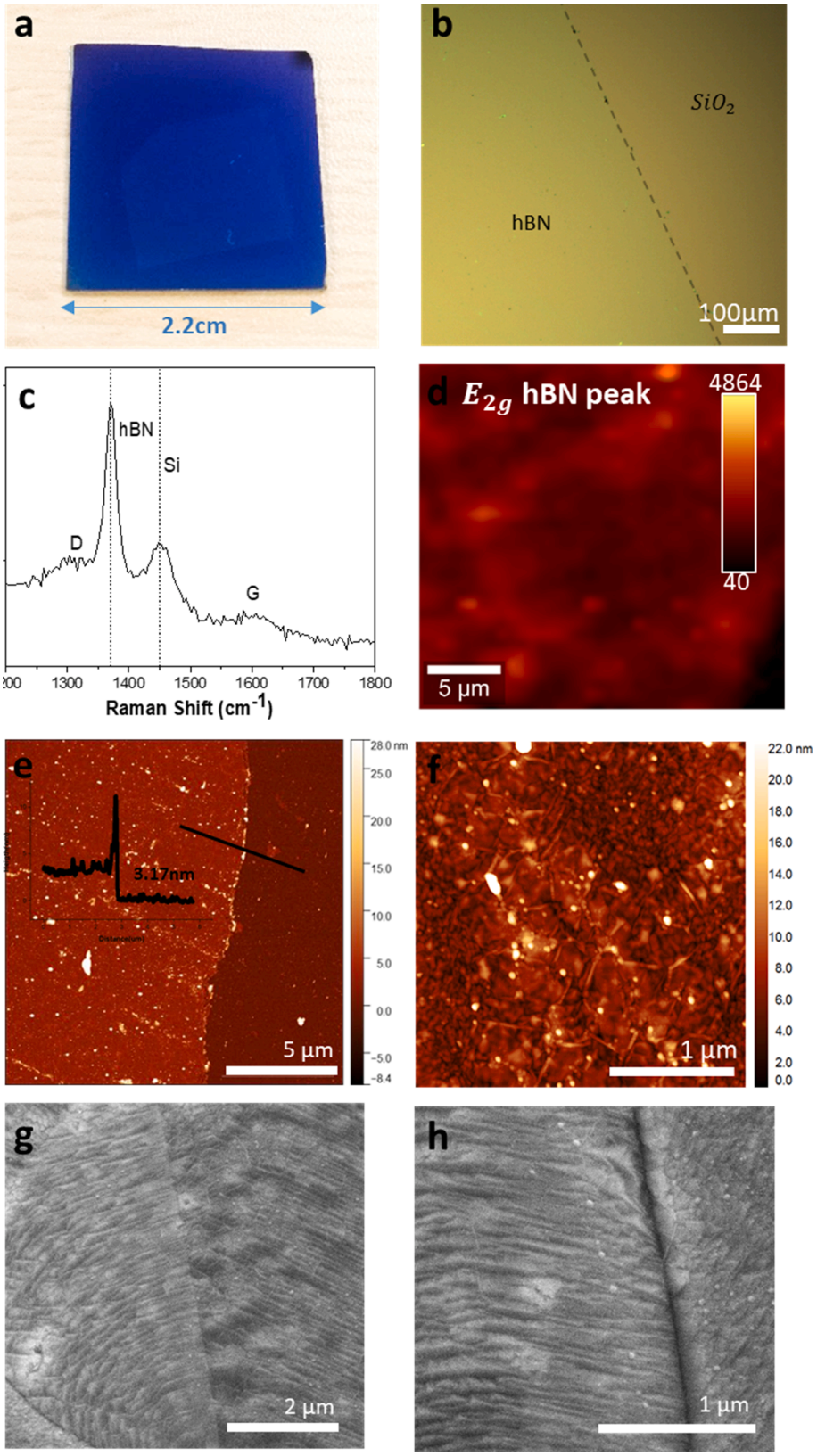

Fig. 2. a) Photograph of the transferred hBN film over a SiO_2 substrate. b) OM image of the grown film. c) Representative Raman spectra of the sample. d) Raman map tracking the intensity of the E_{2g} hBN peak in the 1350–1385 cm^{-1} range. The map is taken on 45 x 45 points in a 30 x 30 μm^2 area. e) AFM and line scan profile of the hBN film. f) AFM close-up image of the hBN film. g-h) SEM images of the hBN film on Cu foil substrate.

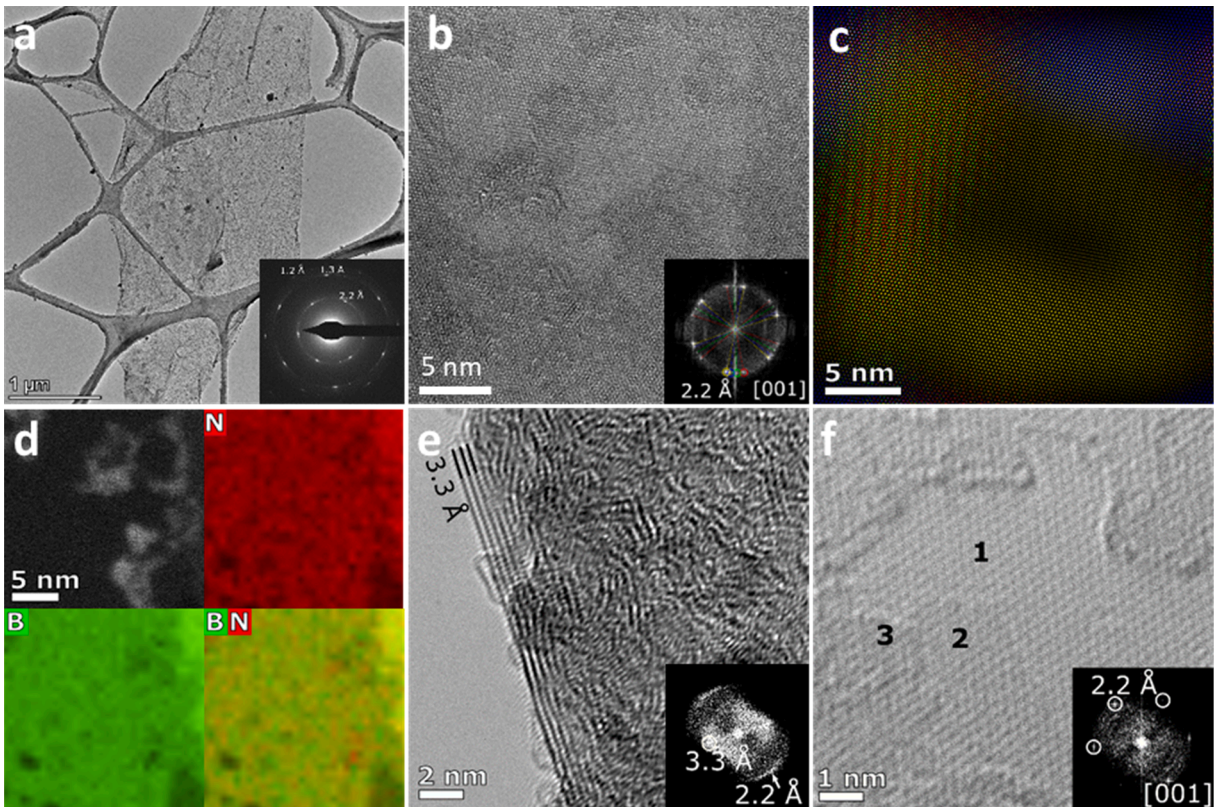

Fig. 3. TEM characterization of hBN films. a) TEM image of the hBN polycrystalline film with electron diffraction (inset), showing the majority of the reflections coming from the [0 0 1] zone axis of hBN. b) High-resolution TEM image of the hBN film with the corresponding FFT (inset): the colored circles indicate the 2.2 Å d-spacing of the (1 0 0) planes of the [0 0 1] zone axis, with the FFT indicating four distinct zone axes with slight tilts from each other. c) Inverted FFT of the red, blue, green and red spots from the four separate layers and reflections in image. d) STEM micrograph of the hBN film and corresponding EELS elemental maps for B, N and the overlapping signal. e) and f) High-resolution TEM image of the hBN film, with e) showing the interlayer spacing of 3.3 Å, corresponding to the (0 0 2) planes of hBN and f) showing three layers of hBN (numbered 1–3), and FFT indexed to [0 0 1] zone axis (inset).

and 398.6 eV (in B1s and N1s, respectively) can be associated to monolayer hBN (or to local cubic-like sp^3 coordination) [47,48]. The components at 190.6 and 398.1 eV can be associated to multilayer hBN. The third component at 192.1 and 399.3 eV can instead be associated with defects. By analyzing the component intensities and ratios, the CVD spectrum indicates the prevalence of multilayer hBN (the multilayer/monolayer intensity ratio is ~2 for both B1s and N1s). Interestingly, the defects are mainly concentrated on boron, while the defect-related component of nitrogen is almost negligible. The analysis of the LPE spectral features leads to a consistently different situation. Here, the monolayer-related components are more intense than the multilayer ones by a ~3.4 factor. Differently from the CVD sample, the defects are linked to both elements.

After the complete characterization of the structural and compositional properties of the hBN samples, we studied the fluorescence emission. TIRFM and confocal fluorescence images collected for CVD and LPE hBN samples are shown in Fig. 6. Notably, no surface modification via FIB or plasma exposure was necessary to induce fluorescent emission, showing that the crystal defects in hBN are naturally occurring in both CVD and LPE samples. SPE signatures appear as intensity spots with a shape matching the point spread function (PSF) of the microscope. This match was further verified by performing Gaussian fittings of the intensity profiles across individual spots. The measured full-width at half maximum (FWHM) are 218 ± 18 nm and 222 ± 17 nm for CVD and LPE samples, respectively (insets in Fig. 6c and f). Both values match the diffraction-limited spot size of the microscope (*i.e.*, 220 nm). We remark that, considering the laser cleaning we used (see section 2.4.8) and the fact that photo-bleaching of molecules should take seconds to minutes [49,50], we are confident that the measured signals are not originating from adsorbed molecules. Other evidence also support that the observed emission in the two kinds of samples is inherent to hBN: i) the observed PSF shape is in line with a single dipole emitter, ii) the emission is persistent over long excitation times (up to tens of minutes), iii) the spectral signatures of both kinds of samples in line with existing literature (see Table 1).

Our hyperspectral confocal microscope images provide spectrally resolved fluorescence emission information. We analyzed several categories of spectral fingerprints associated with the pixel colors in the images. The signature emission peaks (typically referred to as zero phonon lines – ZPL) were used to analyze the images (Fig. 6h and i): They are located at ~538, 582, and 617 nm for the CVD samples, and ~529, 573, and 617 nm for the LPE samples. We attribute this difference in emission wavelength to the kind of crystal lattice defect, which could be a substitution of a few types (*e.g.*, H and O atom), a B vacancy or a C

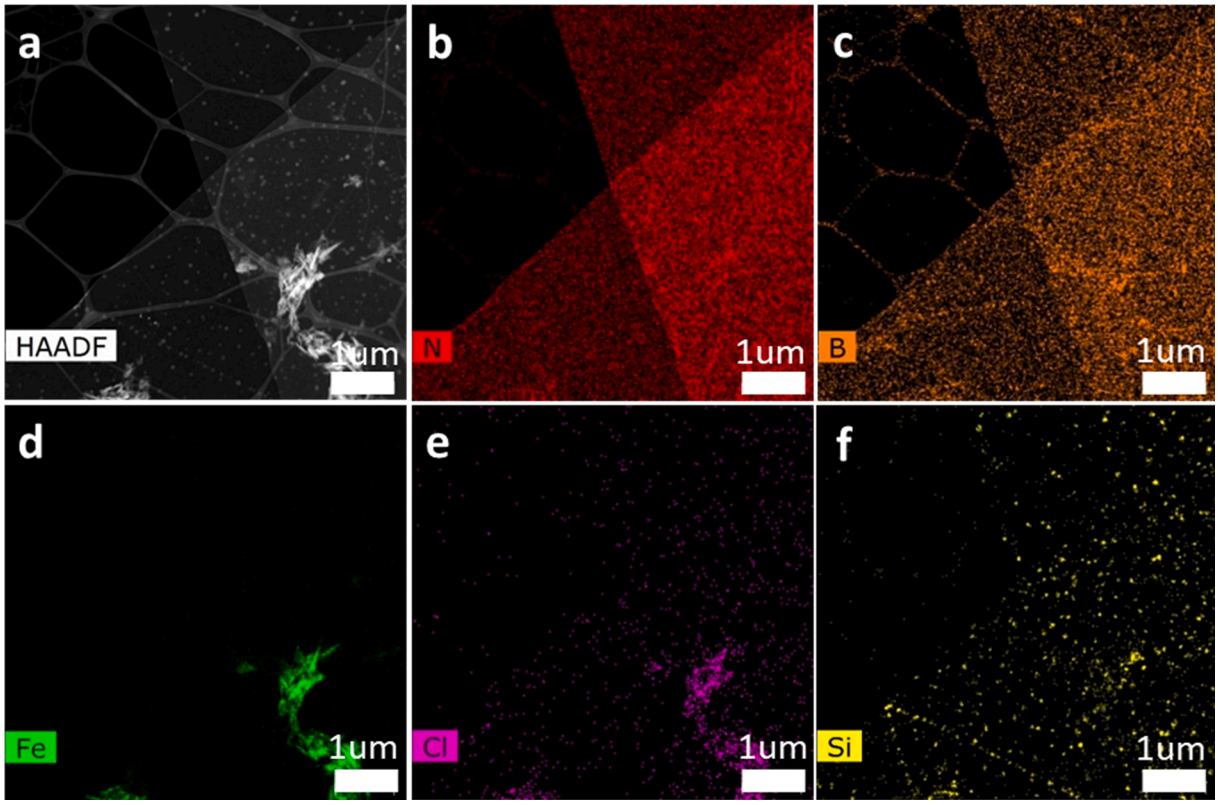

Fig. 4. Elemental analysis of the hBN sample by EDS. a) HAADF-STEM and b)-f) corresponding N, B, Fe, Cl, and Si elemental EDS mapping.

interstitial defect [51,52]. Furthermore, we can safely claim that the observed emission peaks are not an hBN Raman shift, which is at ~523 nm for the excitation wavelength of 488 nm. In a minority of images, the ZPL positions appeared slightly shifted from the rest, probably due to local strain in the hBN film, as reported in recent studies [53–55]. Similarly large spectral ranges were also previously reported [18,20,55]. We also observed several replica peaks, typically called phonon side bands (PSBs), whose wavelength difference from their respective ZPL is $\Delta\lambda = 45.7 \pm 6.5$ nm, in agreement with the literature [23,24,56]. Interestingly, at times the intensity spots show deviations from a circular shape: They appear also as half circles and single lines/stripes (white and magenta arrows, respectively, in Fig. 6c and f). These shapes are usually indications of "blinking", *i.e.*, a fluorescence intermittency due to emitter transitions between long-lived (ms to s) dark and bright states [23,57]. The different spot shape is thus determined by the average duration of the bright and dark states, due to the laser scanning nature of the confocal measurement. Blinking is generally undesirable, since highly stable emitters are required for any operating SPE device [13]. This behavior, observed also in single molecule and quantum dot emitters [20,58], still needs to be fully understood, although the suspected cause is random environment-dependent fluctuations of the local electric field of surface defects [57,59].

The time scales for the fluorescent intermittency were obtained by analyzing the intensity profiles over time extracted from the TIRFM recordings for 280 intermittent emitters in the CVD sample (Fig. 7a). From these 280 emitters, 85 demonstrated flickering behavior: the emitter bright state duration spanned from 50 ms (minimum time bin used) to 7.2 s. The dwell time distribution of these intervals follows a power law (Fig. 7b), as commonly observed for fluorescent hBN point defects [57,60], as well as quantum dots [61] and single molecule quantum emitters [62]. The minimum time scale is expected to be lower (a few ns [63]), but it was limited by the exposure time used during the TIRFM recordings (50 ms). Likewise, this analysis was carried out considering 36 intermittent emitters from the LPE sample (Fig. 7c and d).

We analyzed the emitter density by determining the number of well-isolated diffraction-limited spots per unit area in widefield TIRF fluorescence images. In this way, the values reflect the density of fluorescent emitters usable in quantum photonic applications, where addressing individual emitters is crucial [64]. CVD and LPE hBN have similar emitter densities: 0.09 ± 0.01 and 0.13 ± 0.02 emitters/μm^2, respectively, corresponding to a mean distance between emitters of 3.25 ± 0.21 and 2.73 ± 0.27 μm. This is a significant similarity between the two samples.

Discussion

hBN of the highest quality is usually grown by LPCVD. In that case, the growth is generally surface-reaction-limited and thus less affected by the substrate morphology and the gas flow conditions: Large-area hBN

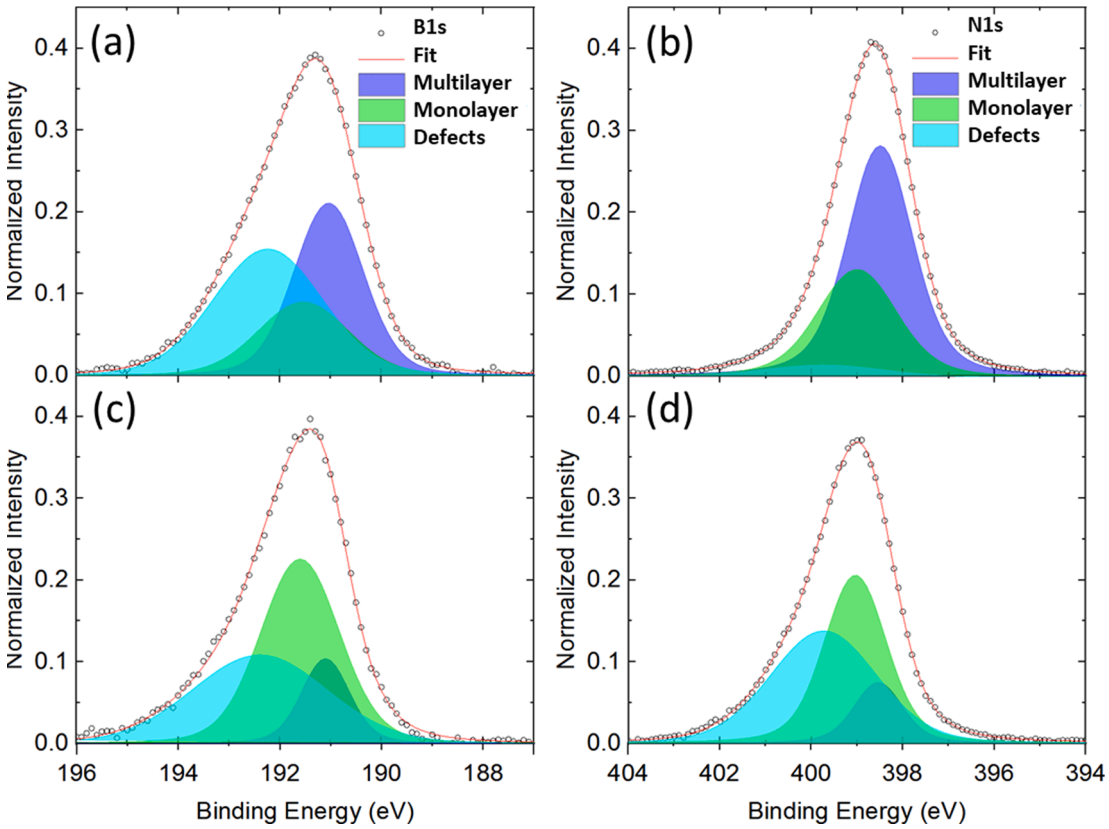

Fig. 5. B1s and N1s core level peaks for the CVD sample (a-b) and LPE sample (c-d). The fit component are pointed out in the spectra deconvolution.

was grown on Cu as monolayer (with AB precursor) [65] and few- to multilayer films (with ammonia and diborane precursors) [66]. Chen et al. reported the epitaxial growth of single-crystal, monolayer hBN on 2″ sapphire/Cu (1 1 1) (500 nm) substrates (~20 cm^2) [67]. Remarkably, Wang et al. was able to further scale-up the production by achieving epitaxial growth of single-crystal, monolayer hBN on a 100-cm^2 Cu (1 1 0) surface, by annealing and reconstructing an industrial-grade copper foil [68]. By contrast, to date only a few groups grew hBN by APCVD on Cu, using in all cases AB as precursor. Monolayer hBN grains with limited sizes were reported in two cases (sizes of ~35 [69] and 80 μm^2 [70]). Three groups reported hBN polycrystalline films with various thickness: i), atomic-thick (*i.e.*, two to five layers [71]), ii) 2 nm [72], iii) "ultrathin" [70]. Stehle et al. reported the growth of monolayer hBN films on electropolished Cu foils (~25 cm^2) [73]. At atmospheric pressure, the nucleation density and domain size are highly dependent on the surface morphology and oxygen content of the Cu substrate [69]. The domain shape, in particular, was found to be affected by the distance between Cu substrate and precursor [73]. The hBN growth is known to follow a combination of layer-by-layer growth and island growth model (Stranski–Krastanov growth) [70]. Therefore, longer growth time are expected to produce multilayer hBN films (as we detail in Fig. S6). In our studies, the optimization steps allowed to achieve uniform growth over 20 cm^2 size on untreated Cu foils. The AB pre-treatment tuning stands out as the most effective optimization step which led to uniform samples over extended areas [72].

The SPE density in CVD hBN varies significantly: Some groups reported densities as low as 0.04 emitters/μm^2 [57], while others as high as 2.2 emitters/ μm^2 [23]. The emitter density of 0.09 ± 0.01 emitters/ μm^2 determined from our TIRF data falls well within this range. Although high density of SPEs is generally desired for high throughput fabrication of quantum photonic devices, too high densities may pose challenges for the isolation and control of the individual emitters. Emitter densities of 0.33 emitters/ μm^2 at deterministic positions were obtained in hBN via focused ion beam processing [56]. In contrast, our APCVD material possesses emitters at random positions while the density is of similar magnitude, with about 3.5 times fewer emitters per unit area and sufficient average spacing between emitter fluorescence spots to distinguish them using far-field microscopy techniques. The many approaches tried in the search of an ideal hBN SPE platform (controlling emitter density by FIB exposure [56] and by nano-pillar fabrication over the growth substrate [44], stabilization of fluorescence intermittency by surface passivation [59] and bias voltage [23], and homogenization of the defect type by carbon-containing precursors [52] and LPCVD parameter fine tuning [23]) have the downsides of added complexity and higher cost. Our APCVD hBN was produced by the combination of versatile substrate preparation and growth method using a non-toxic

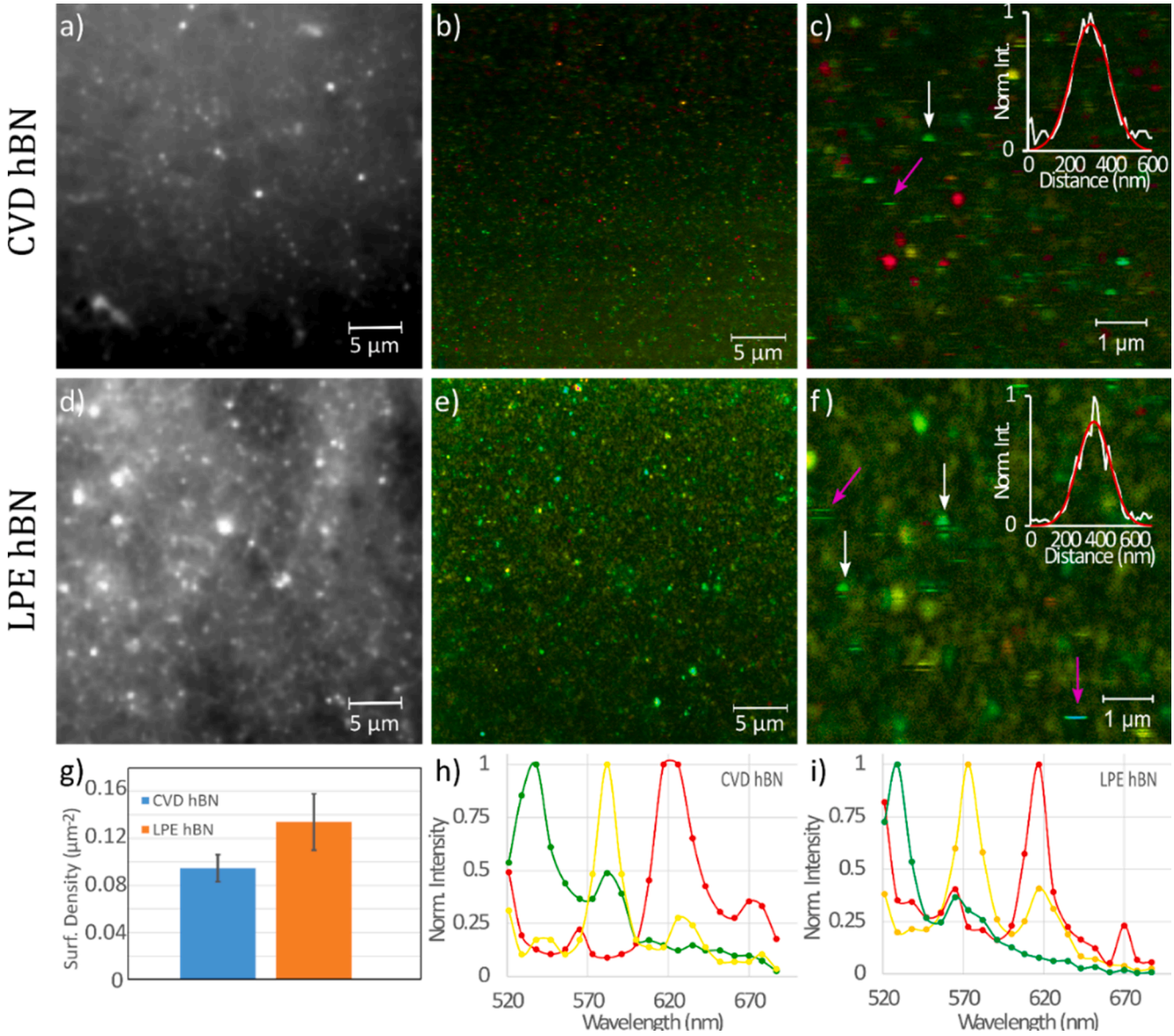

Fig. 6. Fluorescence intensity and spectral analysis of the two hBN samples. Panels a), b), and c) pertain CVD hBN, as follows: (a) fluorescence intensity image as observed by TIRFM, (b) hyperspectral confocal fluorescence image (the colors correlate to the recorded spectral components at each pixel), (c) zoomed-in confocal fluorescent image with inset illustrating the intensity profile of one fluorescent spot and its Gaussian fitting. Panels d), e), and f) represent the same information for LPE hBN. In the confocal images (over 33.7 x 33.7 μm^2 areas), the density appeared as 0.68 ± 0.15 and 0.23 ± 0.05 emitters/μm^2, respectively. The difference with the TIRF measurements is related to a lower counting accuracy in the confocal microscopy data, due to noise artefacts in the automatic counting algorithm (see section 2.4.8). Panel g) represents the mean emitter surface density values extracted for both samples using the TIRFM system. Panels h) and i) reveal the most representative spectra observed in each sample.

precursor. The samples showed a reasonably high emitter density, making the APCVD method viable for the production of large SPE samples. In Table 1, we summarize the observations made for the fluorescent emission in comparison to literature data. The emission peak positions are also in line with previous data, which range between 575 and 585 nm. Minor differences between the ZPL positions may be attributed to the fact that fluorescence emitters in hBN are environment-sensitive [74]: Charge traps and different strain induced by diverse substrates could alter the ZPL position by a few nm [52].

Since the emitters observed in CVD and LPE hBN exhibit the same spectral components, we conclude that the CVD process is not incorporating unexpected impurities into the material, which would show in the measured spectral features [57]. This is a proof of the CVD material's quality, when considering that LPE hBN flakes are generally regarded as a viable type of hBN for nano-photonic applications [18,76,77]. Regarding single-photon emission in hBN, the exact mechanism and the nature of the emission centers remain a subject of investigation, with several kinds of defects proposed as sources [11,12]. Overall, our results

Table 1
SPE features as observed in recent works on CVD hBN. MP and PSB stand for main peak and phonon side band, respectively. *Carbon doping was performed during the growth.

Ref	Growth method	Substrate	Pre-treatment	Sample feature	SPE density (emitters/μm^2)	Emission Peaks (nm). ZPL/PSB1/PSB2
This work	APCVD	Borosilicate glass	NA	~3 nm (~5–10 layers)	0.09 ± 0.01	538/582/NA 582/626/NA 621/670/NA
This work	LPE	Borosilicate glass	NA	4 nm	0.13 ± 0.02	529/565/NA 573/617/NA 617/670/NA
[52]	MBE	Sapphire Carbon doping*	NA ~18 nm	~20 nm 5–8	NA 570–770/NA/NA	NA/NA/NA
[23]	CVD	SiO_2/Si	NA	1.4–2.7 nm thickness	Overall emitter density/single emitter = 2.2/0.84	580 ± 10/628.5/NA
[57]	CVD	Glass	NA	Monolayer	0.04	575 ± 15 /NA/NA
[56]	CVD	SiO_2	FIB and annealing	~15 layers	0.33	575/616/NA
[11]	CVD LPE	Si Si	NA Annealing	Monolayer Multilayer	NA NA	623/NA/NA 623/680/693
[75]	LPE	Si	Annealing	NA	NA	570 – 770 nm/NA/NA
[63]	LPE	Quartz	Annealing	NA	NA	Four group of emitters (A-D) were distinguished based on the MPs: A: 550–785 nm/NA/NA B: 647–700 nm/NA/NA C: 647–785 nm/NA/NA D: 600–785 nm/NA/NA

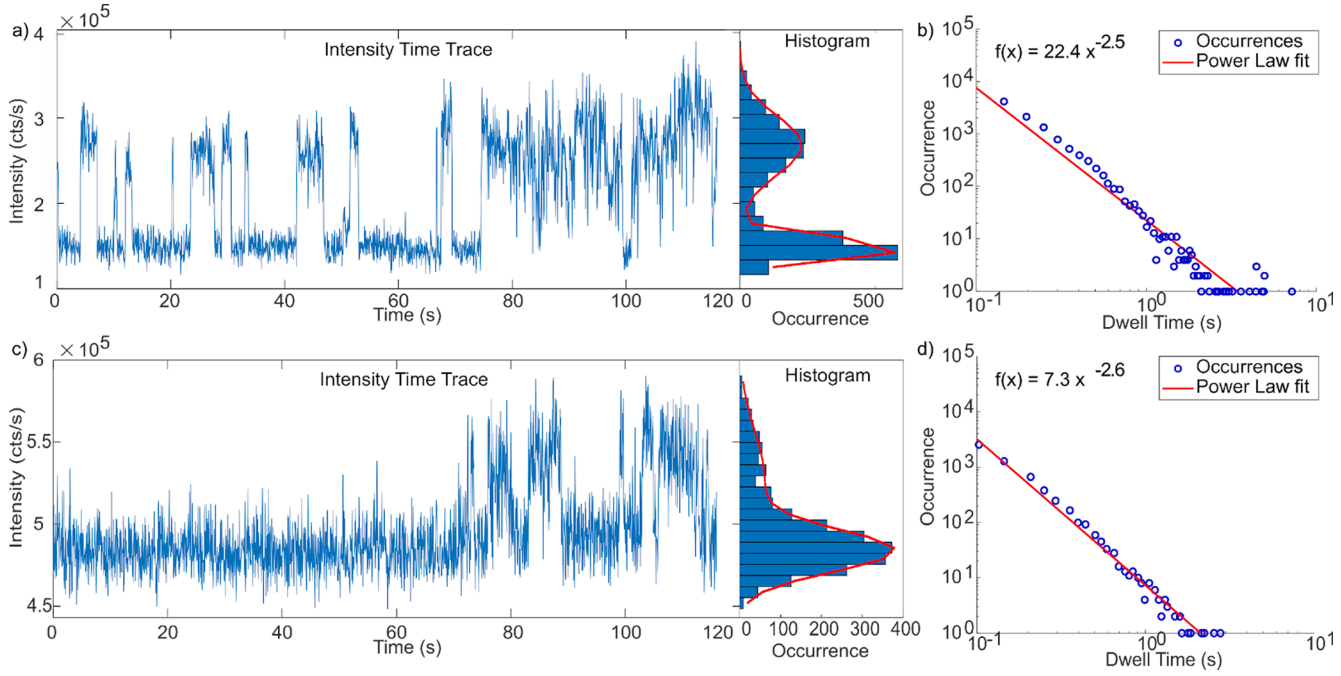

Fig. 7. Fluorescence intermittency behavior of point defects in hBN. a) Fluorescence intensity time trace. The histogram fitted with a double Gaussian curve in red shows the distribution of intensity values across the whole trace revealing a clear distinction between bright and dark states. b) Distribution of the duration times of the bright state for all intermittent emitters recorded. The distribution was fitted to a power law curve whose parameters are displayed in the function f in the inset. c) Example of fluorescence intensity time trace from an emitter in the LPE sample d) Power Law distribution of the bright state duration times for all intermittent emitters the LPE sample.

appear as strong evidence of SPEs in hBN: the observed i) line-shapes, ii) main emission wavelengths, and iii) energy differences between main and red-shifted peaks are all consistent with reported data on SPEs in hBN. The measured fluorescent spots were all confined to the point spread function of the microscope, further indicating that they originate from a point source of light. Finally, the emitters also showed the fluorescence intermittency behavior (following the expected power law statistics) which is commonly found in hBN SPEs.

Conclusions

We presented a robust method for the production of uniform, centimeter-scale, few-layer hBN films, as a suitable and facile alternative to usual top-down methods. By optimizing the pre-conditions and entire parameter set of an atmospheric-pressure CVD process, we reproducibly grew hBN films up to 20 cm^2 size (corresponding to a 2″ wafer). After the growth, the films were transferred to target substrates for a wide range of characterizations. The hBN films are uniform and with an average ~3

nm thickness. EDX and XPS analyses highlighted the general purity of the grown material. The fluorescence emission properties of the CVD hBN film were measured by total internal reflection fluorescence microscopy and confocal fluorescence microscopy, and compared to those of pristine hBN flakes exfoliated in liquid. Our measurements revealed that the emitters density and spectral features are similar for the two kinds of samples. This indicates that the CVD process is not incorporating additional impurities into the material. The control on sample homogeneity (especially in terms of thickness) over wafer-scale is higher for CVD samples, since LPE samples are inherently made of stacks and clusters of flakes. Considering the observed line-shapes, main emission wavelengths, and peak energy differences, our data constitute a strong evidence of single-photon emission in a wafer-scale hBN film. Therefore, atmospheric pressure CVD represents in perspective a viable and versatile approach to make individually addressable single-photon emitters, which could pave the way to hBN-based quantum photonic devices.

Funding sources

We acknowledge the financial support of i) the project “GEMIS – Graphene-enhanced Electro Magnetic Interference Shielding,” with the reference POCI-01-0247-FEDER-045939, co-funded by COMPETE 2020 – Operational Programme for Competitiveness and Internationalization and FCT –Science and Technology Foundation, under the Portugal 2020 Partnership Agreement, through the European Regional Development Fund (ERDF); ii) the project "Graphene and novel thin films for super-resolution microscopy and bio-sensing" (PTDC/NAN-OPT/29417/2017) financed by ERDF, through the Competitiveness and Internationalization Operational Program (POCI) by Portugal 2020 and by the Portuguese Foundation for Science and Technology (FCT) with references POCI-01-0145-FEDER-029417 and PTDC/NAN-OPT/29417/2017; iii) the FCT in the framework of the Strategic Funding UIDB/04650/2020. One of the authors (T.Q.) acknowledges the FCT financial support under the Quantum Portugal Initiative Ph.D. scholarship SFRH/BD/150646/2020. We acknowledge the support by the INL AEMIS, Micro- and Nanofabrication, and Nanophotonics and Bioimaging research core facilities.

CRediT authorship contribution statement

João Fernandes: Methodology, Investigation, Writing – original draft, Writing – review & editing, Visualization. **Tiago Queirós:** Methodology, Formal analysis, Investigation, Data curation, Writing – review & editing. **João Rodrigues:** Investigation, Writing – review & editing. **Siva Sankar Nemala:** Investigation, Writing – review & editing. **Alec P. LaGrow:** Investigation, Data curation. **Ernesto Placidi:** Investigation, Data curation, Writing – review & editing. **Pedro Alpuim:** Conceptualization, Resources, Supervision, Funding acquisition. **Jana B. Nieder:** Conceptualization, Methodology, Writing – review & editing, Project administration, Funding acquisition. **Andrea Capasso:** Conceptualization, Methodology, Validation, Writing – review & editing, Visualization, Supervision, Project administration, Funding acquisition.

Declaration of Competing Interest

The authors declare that they have no known competing financial interests or personal relationships that could have appeared to influence the work reported in this paper.

Appendix A. Supplementary data

Supplementary data to this article can be found online at https://doi.org/10.1016/j.flatc.2022.100366.

References

[1] S. Kang, D. Lee, J. Kim, et al., 2D semiconducting materials for electronic and optoelectronic applications: Potential and challenge, 2D Mater. 7 (2) (2020) 022003, https://doi.org/10.1088/2053-1583/ab6267.
[2] H. Liu, J. Meng, X. Zhang, Y. Chen, Z. Yin, D. Wang, Y.e. Wang, J. You, M. Gao, P. Jin, High-performance deep ultraviolet photodetectors based on few-layer hexagonal boron nitride, Nanoscale. 10 (12) (2018) 5559–5565.
[3] Q.A. Vu, J.H. Lee, V.L. Nguyen, Y.S. Shin, S.C. Lim, K. Lee, J. Heo, S. Park, K. Kim, Y.H. Lee, W.J. Yu, Tuning carrier tunneling in van der Waals heterostructures for ultrahigh detectivity, Nano Lett. 17 (1) (2017) 453–459.
[4] S. Veeralingam, L. Durai, P. Yadav, S. Badhulika, Record-high responsivity and detectivity of a flexible deep-ultraviolet photodetector based on solid state-assisted synthesized hBN nanosheets, ACS Appl. Electron. Mater. 3 (3) (2021) 1162–1169, https://doi.org/10.1021/acsaelm.0c01021.
[5] G. Cassabois, P. Valvin, B. Gil, Hexagonal boron nitride is an indirect bandgap semiconductor, Nat. Photonics 10 (4) (2016) 262–266, https://doi.org/10.1038/nphoton.2015.277.
[6] C. Elias, P. Valvin, T. Pelini, A. Summerfield, C.J. Mellor, T.S. Cheng, L. Eaves, C. T. Foxon, P.H. Beton, S.V. Novikov, B. Gil, G. Cassabois, Direct band-gap crossover in epitaxial monolayer boron nitride, Nat. Commun. 10 (1) (2019), https://doi.org/10.1038/s41467-019-10610-5.
[7] K. Zhang, Y. Feng, F. Wang, Z. Yang, J. Wang, Two dimensional hexagonal boron nitride (2D-hBN): Synthesis, properties and applications, J. Mater. Chem. C 5 (46) (2017) 11992–12022, https://doi.org/10.1039/c7tc04300g.
[8] Y. Kubota, K. Watanabe, O. Tsuda, T. Taniguchi, Deep ultraviolet light-emitting hexagonal boron nitride synthesized at atmospheric pressure, Science (80-) 317 (5840) (2007) 932–934, https://doi.org/10.1126/science.1144216.
[9] L. Wang, B. Wu, J. Chen, H. Liu, P. Hu, Y. Liu, Field-Effect Transistors: Monolayer Hexagonal Boron Nitride Films with Large Domain Size and Clean Interface for Enhancing the Mobility of Graphene-Based Field-Effect Transistors (Adv. Mater. 10/2014), Adv. Mater. 26 (10) (2014) 1474.
[10] L. Britnell, R.V. Gorbachev, R. Jalil, et al., Atomically thin boron nitride : a tunnelling barrier for graphene devices, Engineering. 12 (3) (2012) 7.
[11] T.T. Tran, K. Bray, M.J. Ford, M. Toth, I. Aharonovich, Quantum emission from hexagonal boron nitride monolayers, Nat. Nanotechnol. 11 (1) (2016) 37–41, https://doi.org/10.1038/nnano.2015.242.
[12] S.A. Tawfik, S. Ali, M. Fronzi, M. Kianinia, T.T. Tran, C. Stampfl, I. Aharonovich, M. Toth, M.J. Ford, First-principles investigation of quantum emission from hBN defects, Nanoscale. 9 (36) (2017) 13575–13582.
[13] I. Aharonovich, D. Englund, M. Toth, Solid-state single-photon emitters, Nat. Photonics 10 (10) (2016) 631–641, https://doi.org/10.1038/nphoton.2016.186.
[14] M. Atatüre, D. Englund, N. Vamivakas, S.Y. Lee, J. Wrachtrup, Material platforms for spin-based photonic quantum technologies, Nat. Rev. Mater. 3 (5) (2018) 38–51, https://doi.org/10.1038/s41578-018-0008-9.
[15] S.I. Azzam, K. Parto, G. Moody, Prospects and challenges of quantum emitters in 2D materials, Appl. Phys. Lett. 118 (24) (2021), 240502, https://doi.org/10.1063/5.0054116.
[16] J.J.P. Thompson, S. Brem, H. Fang, J. Frey, S.P. Dash, W. Wieczorek, E. Malic, Criteria for deterministic single-photon emission in two-dimensional atomic crystals, Phys Rev Mater. 4 (8) (2020), https://doi.org/10.1103/PhysRevMaterials.4.084006.
[17] M.W. Doherty, N.B. Manson, P. Delaney, F. Jelezko, J. Wrachtrup, L.C. L. Hollenberg, The nitrogen-vacancy colour centre in diamond, Phys. Rep. 528 (1) (2013) 1–45, https://doi.org/10.1016/j.physrep.2013.02.001.
[18] T.T. Tran, C. Elbadawi, D. Totonjian, et al. Robust multicolor single photon emission from point defects in hexagonal boron nitride. *2017 Conf Lasers Electro-Optics, CLEO 2017 - Proc*. 2017;2017-Janua:1-2. 10.1021/acsnano.6b03602.
[19] N.R. Jungwirth, B. Calderon, Y. Ji, M.G. Spencer, M.E. Flatté, G.D. Fuchs, Temperature Dependence of Wavelength Selectable Zero-Phonon Emission from Single Defects in Hexagonal Boron Nitride, Nano Lett. 16 (10) (2016) 6052–6057, https://doi.org/10.1021/acs.nanolett.6b01987.
[20] Z.-Q. Xu, C. Elbadawi, T.T. Tran, M. Kianinia, X. Li, D. Liu, T.B. Hoffman, M. Nguyen, S. Kim, J.H. Edgar, X. Wu, L.i. Song, S. Ali, M. Ford, M. Toth, I. Aharonovich, Single photon emission from plasma treated 2D hexagonal boron nitride, Nanoscale. 10 (17) (2018) 7957–7965.
[21] S. Choi, T.T. Tran, C. Elbadawi, C. Lobo, X. Wang, S. Juodkazis, G. Seniutinas, M. Toth, I. Aharonovich, Engineering and Localization of Quantum Emitters in Large Hexagonal Boron Nitride Layers, ACS Appl. Mater. Interfaces 8 (43) (2016) 29642–29648.
[22] A. Raja, A. Chaves, J. Yu, G. Arefe, H.M. Hill, A.F. Rigosi, T.C. Berkelbach, P. Nagler, C. Schüller, T. Korn, C. Nuckolls, J. Hone, L.E. Brus, T.F. Heinz, D. R. Reichman, A. Chernikov, Coulomb engineering of the bandgap and excitons in two-dimensional materials, Nat. Commun. 8 (1) (2017), https://doi.org/10.1038/ncomms15251.
[23] N. Mendelson, Z.-Q. Xu, T.T. Tran, M. Kianinia, J. Scott, C. Bradac, I. Aharonovich, M. Toth, Engineering and Tuning of Quantum Emitters in Few-Layer Hexagonal Boron Nitride, ACS Nano 13 (3) (2019) 3132–3140.
[24] C. Li, Z.Q. Xu, N. Mendelson, M. Kianinia, M. Toth, I. Aharonovich, Purification of single-photon emission from hBN using post-processing treatments, Nanophotonics. 8 (11) (2019) 2049–2055, https://doi.org/10.1515/nanoph-2019-0099.
[25] M. Torigoe, Y. Kamimura, K. Teii, S. Matsumoto, Effect of low-energy ion impact on the structure of hexagonal boron nitride films studied in surface-wave plasma, Surf. Interface Anal. 51 (1) (2019) 126–130, https://doi.org/10.1002/sia.6573.

[26] P. Arias, A. Ebnonnasir, C.V. Ciobanu, S. Kodambaka, Growth Kinetics of Two-Dimensional Hexagonal Boron Nitride Layers on Pd(111), Nano Lett. 20 (4) (2020) 2886–2891, https://doi.org/10.1021/acs.nanolett.0c00704.

[27] Z. Shi, X. Wang, Q. Li, P. Yang, G. Lu, R. Jiang, H. Wang, C. Zhang, C. Cong, Z. Liu, T. Wu, H. Wang, Q. Yu, X. Xie, Vapor–liquid–solid growth of large-area multilayer hexagonal boron nitride on dielectric substrates, Nat. Commun. 11 (1) (2020), https://doi.org/10.1038/s41467-020-14596-3.

[28] M.H. Khan, H.K. Liu, X. Sun, Y. Yamauchi, Y. Bando, D. Golberg, Z. Huang, Few-atomic-layered hexagonal boron nitride: CVD growth, characterization, and applications, Mater. Today 20 (10) (2017) 611–628.

[29] W. Auwärter, Hexagonal boron nitride monolayers on metal supports: Versatile templates for atoms, molecules and nanostructures, Surf. Sci. Rep. 74 (1) (2019) 1–95, https://doi.org/10.1016/j.surfrep.2018.10.001.

[30] B. Sompalle, J. Borme, F. Cerqueira, T. Sun, R. Campos, P. Alpuim, Chemical vapour deposition of hexagonal boron nitride for two dimensional electronics, UPorto J. Eng. 3 (3) (2017) 27–34, https://doi.org/10.24840/2183-6493_003.003_0003.

[31] J.C. Koepke, J.D. Wood, Y. Chen, S.W. Schmucker, X. Liu, N.N. Chang, L. Nienhaus, J.W. Do, E.A. Carrion, J. Hewaparakrama, A. Rangarajan, I. Datye, R. Mehta, R. T. Haasch, M. Gruebele, G.S. Girolami, E. Pop, J.W. Lyding, Role of pressure in the growth of hexagonal boron nitride thin films from ammonia-borane, Chem. Mater. 28 (12) (2016) 4169–4179.

[32] X. Li, Y. Zhu, W. Cai, M. Borysiak, B. Han, D. Chen, R.D. Piner, L. Colombo, R. S. Ruoff, Transfer of large-area graphene films for high-performance transparent conductive electrodes, Nano Lett. 9 (12) (2009) 4359–4363.

[33] K.H. Lee, H.-J. Shin, J. Lee, I.-Y. Lee, G.-H. Kim, J.-Y. Choi, S.-W. Kim, Large-scale synthesis of high-quality hexagonal boron nitride nanosheets for large-area graphene electronics, Published online 12 (2) (2012) 714–718.

[34] V. Babenko, G. Lane, A.A. Koos, A.T. Murdock, K. So, J. Britton, S.S. Meysami, J. Moffat, N. Grobert, Time dependent decomposition of ammonia borane for the controlled production of 2D hexagonal boron nitride, Sci. Rep. 7 (1) (2017), https://doi.org/10.1038/s41598-017-14663-8.

[35] B. Sompalle, C.-D. Liao, B. Wei, M. Cerqueira, N. Nicoara, Z. Wang, S. Sadewasser, P. Alpuim, Role of sublimation kinetics of ammonia borane in chemical vapor deposition of uniform, large-area hexagonal boron nitride, J. Vac. Sci. Technol., A 39 (4) (2021) 042202.

[36] Selective Defect Formation in Hexagonal Boron Nitride. Published online 2007.

[37] A. Gnisci, G. Faggio, G. Messina, J. Kwon, J.-Y. Lee, G.-H. Lee, T. Dikonimos, N. Lisi, A. Capasso, Ethanol-CVD Growth of Sub-mm Single-Crystal Graphene on Flat Cu Surfaces, J. Phys. Chem. C 122 (50) (2018) 28830–28838.

[38] P. Gagare, Ammonia borane-hydrogen cycle: Synthesis, dehydrogenation and regeneration, ETD Collect Purdue Univ, Published online, 2009.

[39] M.H. Khan, G. Casillas, D.R.G. Mitchell, H.K. Liu, L. Jiang, Z. Huang, Carbon- and crack-free growth of hexagonal boron nitride nanosheets and their uncommon stacking order, Nanoscale. 8 (35) (2016) 15926–15933, https://doi.org/10.1039/c6nr04734c.

[40] Y. Wen, X. Shang, J. Dong, K. Xu, J. He, C. Jiang, Ultraclean and large-area monolayer hexagonal boron nitride on Cu foil using chemical vapor deposition, Nanotechnology. 26 (27) (2015) 275601.

[41] R.V. Gorbachev, I. Riaz, R.R. Nair, et al., Hunting for Monolayer Boron Nitride: Optical and Raman Signatures, Small 7 (4) (2011) 465–468, https://doi.org/10.1002/smll.201001628.

[42] C. Wu, A.M. Soomro, F. Sun, et al., Large-roll growth of 25-inch hexagonal BN monolayer film for self-release buffer layer of free-standing GaN wafer, Sci. Rep. 6 (October) (2016) 1–9, https://doi.org/10.1038/srep34766.

[43] N. Lisi, T. Dikonimos, F. Buonocore, et al., Contamination-free graphene by chemical vapor deposition in quartz furnaces, Sci. Rep. 7 (1) (2017) 9927, https://doi.org/10.1038/s41598-017-09811-z.

[44] C. Li, N. Mendelson, R. Ritika, Y. Chen, Z. Xu, M. Toth. Scalable and Deterministic Fabrication of Quantum Emitter Arrays from Hexagonal Boron Nitride. 2007;(Cvd): 25-28.

[45] A.B.D. Shaik, P. Palla, Optical quantum technologies with hexagonal boron nitride single photon sources, Sci. Rep. 11 (1) (2021) 1–27, https://doi.org/10.1038/s41598-021-90804-4.

[46] P.R. Kidambi, R. Blume, J. Kling, et al., In situ observations during chemical vapor deposition of hexagonal boron nitride on polycrystalline copper, Chem. Mater. 26 (22) (2014) 6380–6392, https://doi.org/10.1021/cm502603n.

[47] J. Deng, G. Chen, X. Song, Characterization of cubic boron nitride thin films deposited by RF sputter, Int. J. Mod Phys B 16 (28–29) (2002) 4339–4342, https://doi.org/10.1142/s021797920201539x.

[48] R. Trehan, Y. Lifshitz, J.W. Rabalais, Auger and x-ray electron spectroscopy studies of h BN, c BN, and N + 2 ion irradiation of boron and boron nitride, J. Vac. Sci. Technol. A Vacuum, Surfaces, Film. 8 (6) (1990) 4026–4032, https://doi.org/10.1116/1.576471.

[49] C. Liesche, K.S. Grußmayer, M. Ludwig, et al., Automated analysis of single-molecule photobleaching data by statistical modeling of spot populations, Biophys. J . 109 (11) (2015) 2352–2362, https://doi.org/10.1016/j.bpj.2015.10.035.

[50] S. Dey, S. Maiti, Single-molecule photobleaching: Instrumentation and applications, J. Biosci. 43 (3) (2018) 447–454, https://doi.org/10.1007/s12038-018-9770-5.

[51] Q. Tan, J. Lai, X. Liu, Y. Xue, X. Dou. Robust Ultraviolet to Near-infrared Quantum Emitters in Hexagonal Boron Nitride up to 1100 K. :11-13.

[52] N. Mendelson, D. Chugh, J.R. Reimers, et al. Identifying carbon as the source of visible single-photon emission from hexagonal boron nitride. *Nat. Mater.* 10.1038/s41563-020-00850-y.

[53] G. Grosso, H. Moon, B. Lienhard, et al., Tunable and high-purity room temperature single-photon emission from atomic defects in hexagonal boron nitride, Nat. Commun. 8 (1) (2017), https://doi.org/10.1038/s41467-017-00810-2.

[54] N.V. Proscia, H. Jayakumar, X. Ge, et al., Microcavity-coupled emitters in hexagonal boron nitride, Nanophotonics. 9 (9) (2020) 2937–2944, https://doi.org/10.1515/nanoph-2020-0187.

[55] F. Hayee, L. Yu, J.L. Zhang, et al., Revealing multiple classes of stable quantum emitters in hexagonal boron nitride with correlated optical and electron microscopy, Nat. Mater. 19 (5) (2020) 534–539, https://doi.org/10.1038/s41563-020-0616-9.

[56] J. Ziegler, R. Klaiss, A. Blaikie, D. Miller, V.R. Horowitz, B.J. Alemán, Deterministic quantum emitter formation in hexagonal boron nitride via controlled edge creation, Nano Lett. 19 (3) (2019) 2121–2127, https://doi.org/10.1021/acs.nanolett.9b00357.

[57] H.L. Stern, R. Wang, Y. Fan, et al., Spectrally resolved photodynamics of individual emitters in large-area monolayers of hexagonal boron nitride, ACS Nano 13 (4) (2019) 4538–4547, https://doi.org/10.1021/acsnano.9b00274.

[58] J. Hanne, H.J. Falk, F. Görlitz, et al., STED nanoscopy with fluorescent quantum dots, Nat. Commun. 6 (1) (2015) 7127, https://doi.org/10.1038/ncomms8127.

[59] X. Li, G.D. Shepard, A. Cupo, et al., Nonmagnetic quantum emitters in boron nitride with ultranarrow and sideband-free emission spectra, ACS Nano 11 (7) (2017) 6652–6660, https://doi.org/10.1021/acsnano.7b00638.

[60] J. Comtet, E. Glushkov, V. Navikas, et al., Wide-field spectral super-resolution mapping of optically active defects in hexagonal boron nitride, Nano Lett. 19 (4) (2019) 2516–2523, https://doi.org/10.1021/acs.nanolett.9b00178.

[61] P. Bharadwaj, L. Novotny, Robustness of quantum dot power-law blinking, Nano Lett. 11 (5) (2011) 2137–2141, https://doi.org/10.1021/nl200782v.

[62] M. Haase, C.G. Hübner, E. Reuther, A. Herrmann, K. Müllen, T. Basché, Exponential and power-law kinetics in single-molecule fluorescence intermittency, J. Phys. Chem. B 108 (29) (2004) 10445–10450, https://doi.org/10.1021/jp0313674.

[63] M.K. Boll, I.P. Radko, A. Huck, U.L. Andersen, Photophysics of quantum emitters in hexagonal boron-nitride nano-flakes, Opt. Express 28 (5) (2020) 7475, https://doi.org/10.1364/oe.386629.

[64] J. Lee, V. Leong, D. Kalashnikov, J. Dai, A. Gandhi, L. Krivitsky. Integrated Single Photon Emitters. Published online 2020:1-46.

[65] K.K. Kim, A. Hsu, X. Jia, et al., Synthesis of monolayer hexagonal boron nitride on Cu foil using chemical vapor deposition, Nano Lett. 12 (1) (2012) 161–166, https://doi.org/10.1021/nl203249a.

[66] A. Ismach, H. Chou, D.A. Ferrer, et al., Toward the controlled synthesis of hexagonal boron nitride films, ACS Nano 6 (7) (2012) 6378–6385, https://doi.org/10.1021/nn301940k.

[67] T.-A. Chen, C.-P. Chuu, C.-C. Tseng, et al., Wafer-scale single-crystal hexagonal boron nitride monolayers on Cu (111), Nature 579 (7798) (2020) 219–223, https://doi.org/10.1038/s41586-020-2009-2.

[68] L. Wang, X. Xu, L. Zhang, et al., Epitaxial growth of a 100-square-centimetre single-crystal hexagonal boron nitride monolayer on copper, Nature 570 (7759) (2019) 91–95, https://doi.org/10.1038/s41586-019-1226-z.

[69] R.Y. Tay, M.H. Griep, G. Mallick, et al., Growth of large single-crystalline two-dimensional boron nitride hexagons on electropolished copper, Nano Lett. 14 (2) (2014) 839–846, https://doi.org/10.1021/nl404207f.

[70] X. Song, Q. Li, J. Ji, et al., A comprehensive investigation on CVD growth thermokinetics of h-BN white graphene, 2D Mater. 3 (3) (2016), https://doi.org/10.1088/2053-1583/3/3/035007.

[71] L. Song, L. Ci, H. Lu, et al., Large scale growth and characterization of atomic hexagonal boron nitride layers, Nano Lett. 10 (8) (2010) 3209–3215, https://doi.org/10.1021/nl1022139.

[72] R.Y. Tay, X. Wang, S.H. Tsang, et al., A systematic study of the atmospheric pressure growth of large-area hexagonal crystalline boron nitride film, J. Mater. Chem. C 2 (9) (2014) 1650–1657, https://doi.org/10.1039/c3tc32011a.

[73] Y. Stehle, H.M. Meyer, R.R. Unocic, et al., Synthesis of hexagonal boron nitride monolayer: control of nucleation and crystal morphology, Chem. Mater. 27 (23) (2015) 8041–8047, https://doi.org/10.1021/acs.chemmater.5b03607.

[74] B. Sontheimer, M. Braun, N. Nikolay, N. Sadzak, I. Aharonovich, O. Benson, Photodynamics of quantum emitters in hexagonal boron nitride revealed by low-temperature spectroscopy, Phys Rev B. 96 (12) (2017) 1–5, https://doi.org/10.1103/PhysRevB.96.121202.

[75] T.T. Tran, M. Kianinia, M. Nguyen, et al., Resonant excitation of quantum emitters in hexagonal boron nitride, ACS Photonics 5 (2) (2018) 295–300, https://doi.org/10.1021/acsphotonics.7b00977.

[76] X. Zheng, G. Wang, F. Huang, et al., Liquid Phase Exfoliated Hexagonal Boron Nitride/Graphene Heterostructure Based Electrode Toward Asymmetric Supercapacitor Application, Front. Chem. 7 (August) (2019) 1–9, https://doi.org/10.3389/fchem.2019.00544.

[77] B. Zhang, Q. Wu, H. Yu, et al., High-efficient liquid exfoliation of boron nitride nanosheets using aqueous solution of alkanolamine, Nanoscale Res. Lett. 12 (1) (2017), https://doi.org/10.1186/s11671-017-2366-4.